

# A multi-stage return algorithm for solving the classical damage component of constitutive models for rocks, ceramics, and other rock-like media

R. M. Brannon · S. Leelavanichkul

Received: 27 February 2009 / Accepted: 8 September 2009 / Published online: 25 September 2009  
© Springer Science+Business Media B.V. 2009

**Abstract** Classical plasticity and damage models for porous quasi-brittle media usually suffer from mathematical defects such as non-convergence and non-uniqueness. Yield or damage functions for porous quasi-brittle media often have yield functions with contours so distorted that following those contours to the yield surface in a return algorithm can take the solution to a false elastic domain. A steepest-descent return algorithm must include iterative corrections; otherwise, the solution is non-unique because contours of any yield function are non-unique. A multi-stage algorithm has been developed to address both spurious convergence and non-uniqueness, as well as to improve efficiency. The region of pathological isosurfaces is masked by first returning the stress state to the Drucker–Prager surface circumscribing the actual yield surface. From there, steepest-descent is used to locate a point on the yield surface. This first-stage solution, which is extremely efficient because it is applied in a 2D subspace, is generally not the correct solution, but it is used to estimate the correct return direction. The first-stage solution is projected onto the estimated correct return direction in 6D stress space. Third invariant dependence and anisotropy are accommodated in

this second-stage correction. The projection operation introduces errors associated with yield surface curvature, so the two-stage iteration is applied repeatedly to converge. Regions of extremely high curvature are detected and handled separately using an approximation to vertex theory. The multi-stage return is applied holding internal variables constant to produce a non-hardening solution. To account for hardening from pore collapse (or softening from damage), geometrical arguments are used to clearly illustrate the appropriate scaling of the non-hardening solution needed to obtain the hardening (or softening) solution.

**Keywords** Plasticity · Return algorithms · Rock-like media · Pathologies of yield functions · Damage · Uniqueness

## 1 Introduction

Owing to their simplicity and numerical efficiency, smeared damage models are often used in engineering simulations of fracture and fragmentation. As illustrated in Fig. 1, supplementing a damage model with revisions accounting for uncertainty and scale effects can mitigate mesh sensitivities and improve predictions of irregular localized cracking (Brannon et al. 2007). Given that smeared damage models show this potential for large-scale engineering fracture simulations, robust and efficient solvers are needed that address some

---

R. M. Brannon (✉) · S. Leelavanichkul  
Mechanical Engineering, University of Utah,  
Salt Lake City, UT, USA  
e-mail: rebecca.brannon@utah.edu

S. Leelavanichkul  
e-mail: sleelava@eng.utah.edu

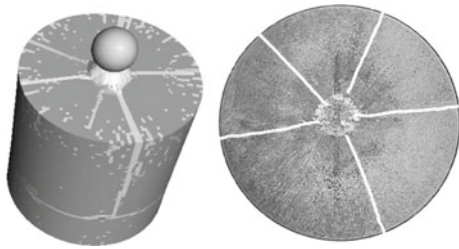


**Fig. 1** Comparison of simulation and experiment for dynamic indentation of silicon-carbide ceramic; the simulation uses a conventional damage model with uncertainty and scale effects in strength and cohesion parameters

of the numerical problems that are common to these plasticity-based damage models.

In plasticity theory, the yield surface is the zero isosurface of the yield function, and negative isosurfaces describe the elastic domain. Isosurfaces are otherwise arbitrary. The isosurfaces in common engineering models for cracked and porous media often have shapes that deviate significantly from the overall shape of the yield surface, which can produce pathological convergence problems in numerical solvers. Nonconvergence or, more insidiously, convergence to an incorrect solution is one of several verification issues that tend to undermine predictiveness of engineering damage models.<sup>1</sup>

For general-purpose plasticity models that support a variety of yield surface shapes, isosurface pathologies can be managed through piecewise differentiable yield functions applied in different zones of stress space. For example, a quasibrittle porous medium (such as rock or concrete) is often modeled using pressure varying strength with a hydrostatic cap to allow pore collapse. These models often have pathological isosurfaces away from the yield surface. However, by using a circumscribing cone, the stress state can be brought to a region of well-behaved yield contours that are subsequently followed to the yield surface.

Solution of the incremental form of classical plasticity equations demands that the updated stress must be a projection of the trial elastic stress onto the yield surface. Regardless of the details of the yield function, the stress must be returned to the yield surface

<sup>1</sup> *Verification*, defined as a confirmation that the governing equations are solved correctly, is distinct from the subsequent process of *validation* to assess appropriateness of the equations to model physical observations (The American Society of Mechanical Engineers 2006).

along a specific trajectory that is uniquely implied by the exact solution of the incremental plasticity equations. Returning the trial stress state to the yield surface along any other trajectory will result in a plasticity algorithm that converges to the wrong result. An expensive six-dimensional return can be replaced with a far more efficient two-dimensional return if the 2-D solution (which is not generally correct) is projected onto the correct 6-D return projection direction as part of a two-stage iterator.

This paper is structured as follows: Sects. 2 and 3 discuss yield function pathologies and review formulas for converting isotropic yield criteria from functions of principal stress to functions of standard invariants, thus simplifying evaluation of yield function gradients. A nested multi-stage return algorithm and an example for returning stress to the yield surface along the proper unique trajectory are then presented in Sects. 4 and 5, where it is also shown that a return algorithm to a stationary (non-hardening) yield surface can be used to return the stress to a moving (hardening or softening) yield surface.

## 2 Pathologies of yield functions

In this paper, we follow the engineering mechanics convention that stress is positive in tension. However, because compression is prevalent in applications, some subsequent expressions might employ an overbar to denote the negative of a quantity. For example,  $\bar{\sigma}_k \equiv -\sigma_k$  and  $\bar{z} \equiv -z$ . In what follows, numerically subscripted eigenvalues  $(\sigma_1, \sigma_2, \sigma_3)$  will *not* be presumed to be ordered. They might reside in any sextant of stress space. If ordered eigenvalues are required, they will be subscripted with “L”, “M”, or “H” (standing for low, middle, and high) so that  $(\sigma_L \leq \sigma_M \leq \sigma_H)$ . The “ordered” principal stresses  $(\sigma_L, \sigma_M, \sigma_H)$  can be expressed in Lode cylindrical coordinates  $(r, \theta, z)$  as follows

$$\begin{aligned}\sigma_L &= \frac{z}{\sqrt{3}} - \frac{r}{\sqrt{2}} \left[ \cos \theta - \frac{\sin \theta}{\sqrt{3}} \right] \\ &= \frac{I_1}{3} - \sqrt{J_2} \left[ \cos \theta - \frac{\sin \theta}{\sqrt{3}} \right]\end{aligned}\quad (1)$$

$$\begin{aligned}\sigma_M &= \frac{z}{\sqrt{3}} - \sqrt{\frac{2}{3}} r \sin \theta \\ &= \frac{I_1}{3} - \frac{2}{\sqrt{3}} \sqrt{J_2} \sin \theta\end{aligned}\quad (2)$$

$$\begin{aligned} \sigma_H &= \frac{z}{\sqrt{3}} + \frac{r}{\sqrt{2}} \left[ \cos \theta + \frac{\sin \theta}{\sqrt{3}} \right] \\ &= \frac{I_1}{3} + \sqrt{J_2} \left[ \cos \theta + \frac{\sin \theta}{\sqrt{3}} \right], \end{aligned} \tag{3}$$

where the Lode coordinates are defined by (Brannon 2007; Lubliner 1990)

$$r = \sqrt{2J_2}, \quad \sin 3\theta = \frac{J_3}{2} \left( \frac{3}{J_2} \right)^{3/2}, \quad z = \frac{I_1}{\sqrt{3}}. \tag{4}$$

The three independent invariants in Eq. 4 are

$$I_1 = \text{tr}\boldsymbol{\sigma} = \sigma_1 + \sigma_2 + \sigma_3 \tag{5}$$

$$J_2 = \frac{1}{2} \text{tr}\mathbf{S}^2 = \frac{1}{2} (s_1^2 + s_2^2 + s_3^2) \tag{6}$$

$$J_3 = \frac{1}{3} \text{tr}\mathbf{S}^3 = \frac{1}{3} (s_1^3 + s_2^3 + s_3^3), \tag{7}$$

where  $\sigma_1, \sigma_2,$  and  $\sigma_3$  are the eigenvalues of the Cauchy stress tensor  $\boldsymbol{\sigma}$ , and  $s_1, s_2,$  and  $s_3$  are the eigenvalues of the stress deviator  $\mathbf{S}$ . The solution for ordered eigenvalues in Eqs. 1–3 may be used to transform any yield or limit function  $f(\sigma_L, \sigma_M, \sigma_H)$  expressed in terms of ordered principal stresses into the form  $f(I_1, J_2, J_3)$  or  $f(r, \theta, z)$ , thereby avoiding expensive eigenvalue analyses and simplifying the evaluation of yield function gradients.

In computational plasticity, the yield function  $f$  must satisfy the following minimal admissibility criteria:

1.  $f < 0$  for elastic states
2.  $f = 0$  on the yield surface
3.  $f > 0$  outside the yield surface

The yield surface is often additionally required to be convex. The yield surface is the “level set” or “iso-surface” corresponding to  $f = 0$ . Isosurfaces corresponding to  $f \neq 0$  are unrestricted as long as the above sign conventions are satisfied. In other words, the yield surface is unique, but the yield function is not unique. For example, the functions  $f(r, \theta, z) = r - k$  and  $f(r, \theta, z) = (r/k)^2 - 1$ , where  $k$  is a constant, both have the same elastic states and yield surfaces. Both functions satisfy the above three admissibility constraints, but these functions are not equal, nor are their gradients equal. Thus, their convergence properties in numerical return algorithms are different. Non-uniqueness of yield functions can lead to pathological problems in numerical plasticity solvers, and this paper suggests additional constraints on yield functions to avoid such problems.

In light of the symmetry properties of isotropic yield functions, it is always possible *in principle* to cast the yield criterion in the form  $r = g(\theta, z)$  for which an admissible yield function could then be simply  $f(r, \theta, z) = r - g(\theta, z)$ . At a given value of the Lode angle  $\theta$ , the meridional profile of the yield surface is described by a function of the form  $r = G(z)$ , where the function  $G$  depends implicitly on the selected “master” Lode angle  $\theta$  at which the meridian is sought. The relationship  $r = G(z)$  may be written more generally in the form  $F(r, z) = 0$ , which, like the general yield function  $f(r, \theta, z)$ , must satisfy  $F < 0$  inside the yield surface and  $F > 0$  outside the yield surface. If a satisfactory meridional yield function  $F(r, z)$  can be found, then the Lode angle dependence may be reintroduced by writing the general yield function as

$$f(r, \theta, z) = F(r\Gamma(\theta, z), z) \tag{8}$$

The function  $\Gamma(\theta, z)$ , which describes the shape of the octahedral yield profile at a given value of  $z$ , must be normalized to equal 1 at the “master” Lode angle so that the meridional profile is defined by  $F(r, z)$  at that angle. A master Lode angle of  $\theta = -30^\circ$  is typically selected because this Lode angle corresponds to axisymmetric compression, where the majority of data is usually available (Fossum and Brannon 2004).

Because computational plasticity models routinely evaluate the yield function at points outside the yield surface, and because the yield function gradient at these points is often needed to return the stress to the yield surface, an essential requirement is that the yield function must have reasonably conforming nonsingular iso-surface contours everywhere. By this, we mean that, for any point in stress space, a return algorithm that moves perpendicular to the isosurfaces must converge to a point on the yield surface. This supplemental admissibility criterion for yield functions does not require the returned stress to necessarily equal the stress state that satisfies the governing equations of plasticity—it only has to be any point on the yield surface. At such a point, where the outward normal to the isosurface is unaffected by ambiguity of yield functions, corrections can be applied to project the returned stress onto the return direction that is uniquely determined from the governing equations. This approach is similar to that of Bicanic and Pearce (1998) except that it is recognized that the correct return direction is *not* to the closest point and the projection must be performed in 6D stress space—not 3D Haigh–Westergaard space—

because the principal directions of the updated stress are generally different from those of the trial stress.

Figure 2 illustrates qualitative distinctions between cracked-only, porous-only and combined crack/pore meridional yield profiles. Research over the past few decades (Sandler and Rubin 1979; Foster et al. 2005) has aimed to describe the combined effect of cracks and pores. Early two-surface models (Sandler and Rubin 1979) achieved a yield profile similar to that in Fig. 2c by simply placing a “cap” (often elliptical in shape) positioned at the critical elastic limit under hydrostatic compression. While being relatively easy to parameterize in terms of standard experiments, this approach leads to a yield function that is not continuously differentiable at the yield surface and often requires iterations for cap placement. An advance over the two-surface approach was introduced by Fossum (Foster et al. 2005), who generated a smoothly differentiable meridional yield profile similar to Fig. 2c by multiplying a fracture function  $r = G_c(z)$  times a normalized (but again elliptical) cap function  $G_p(z)$ .

Fossum’s yield function satisfies the first two yield function admissibility criteria, but it violates the third criterion. In fact, the vast majority of geomaterial yield functions, not just the Fossum function, seem to suffer from this problem. As illustrated in Fig. 3, there exist stress states outside the desired yield surface for which  $f < 0$ . Consequently, checking the sign of these inadmissible yield functions is insufficient for determining if a trial elastic stress state lies outside the yield surface. Moreover, as seen in Fig. 3, there exist regions outside the yield surface for which  $f > 0$  but for which moving perpendicular to yield function contours in a steepest-descent return algorithm would take the stress to the false elastic domain.

Violation of criterion #3 has even been seen in “classical” yield functions such as

$$f = 4J_2^3 - 27J_3^2 - 36k^2J_2^2 + 96k^4J_2 - 64k^6, \quad (9)$$

where  $k$  is a constant. This function is often erroneously claimed to represent the Tresca model (Lubliner 1990). However, as illustrated in Fig. 4a, it violates admissibility criterion #3.

In terms of ordered principal stresses ( $\sigma_L \leq \sigma_M \leq \sigma_H$ ), an admissible yield function for the Tresca criterion is

$$f = (\sigma_H - \sigma_L)/2 - k. \quad (10)$$

By using Eqs. 1–3, this admissible Tresca function may be cast in the form of Eq. 8 as

$$f = \frac{r}{\sqrt{2}} \cos \theta - k, \quad (11)$$

$$f = \sqrt{J_2} \left\{ \cos \left[ \frac{1}{3} \sin^{-1} \left( \frac{J_2}{2} \left( \frac{3}{J_2} \right)^{3/2} \right) \right] \right\} - k. \quad (12)$$

As illustrated in Fig. 4b, all contours for this admissible Tresca yield function are perfect concentric hexagons. Moreover, for a starting point lying anywhere away from the vertices, a Newton iterator will converge to the yield surface in exactly one iteration, or two iterations if the starting point falls within the cone of normals that would make the first iteration move into a new sextant.

The yield function in Eq. 12 is problematic at the hexagon vertices. Even away from those vertices, there is potential for generating a returned state that has a different eigenvalue ordering from that at the starting state (i.e., a change in sextant). Such behavior is undesirable according to Bicanic and Pearce (1998). One way to circumvent these problems, and at the same time salvage the previous inadmissible Eq. 9, is to restrict the domain over which Eq. 9 can be applied. Specifically, one can define

$$f = \begin{cases} 4J_2^3 - 27J_3^2 - 36k^2J_2^2 + 96k^4J_2 - 64k^6 & \text{if } J_2 < \frac{4}{3}k^2 \\ \sqrt{J_2} & \text{if } J_2 > \frac{4}{3}k^2 \end{cases} \quad (13)$$

This discontinuous yield function, illustrated in Fig. 4c, applies the inadmissible function of Eq. 12 only if the stress state falls within the circle circumscribing the Tresca hexagon. Outside this circle, the yield function is of von Mises form. Although unsavory in some respects, using simpler yield functions in this way (i.e., to mask inadmissible domains) is straightforward and expedient, especially when more “clever” yield functions such as that in Eq. 12 are not available. Such is often the case with yield functions for geological materials which have a pronounced vertex on the tensile hydrostat.

Non-uniqueness of yield function isosurfaces will cause non-uniqueness of the answers for any return algorithm that relies exclusively on tracking through yield function contours to reach the yield surface. As mentioned earlier, this non-uniqueness of return algorithms can be removed with a projection correction. Thus, locating the correct point on the yield surface is an iterative process of applying an inexpensive (possibly even 2D) isosurface tracking return algorithm followed by a 6D projection correction. Since the

**Fig. 2** Qualitative meridional profile shapes resulting from **a** porosity alone, **b** microcracks alone, and **c** a combination of porosity and microcracks (Fossum and Brannon 2004)

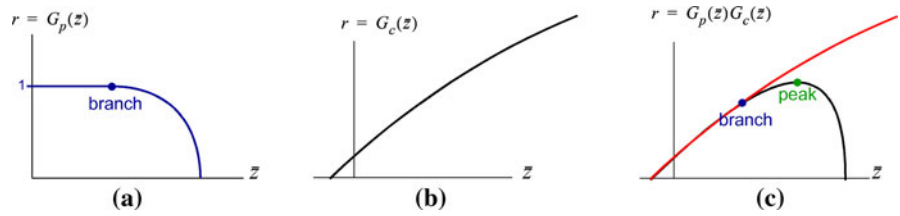


**Fig. 3** Violation of the third admissibility criterion **a** False elastic domains at or near the tensile limit in the meridional plot for a typical geomaterial model. **b** Differences between a desired return location (dashed) and the return location found by moving perpendicular to pathological yield contours (solid)

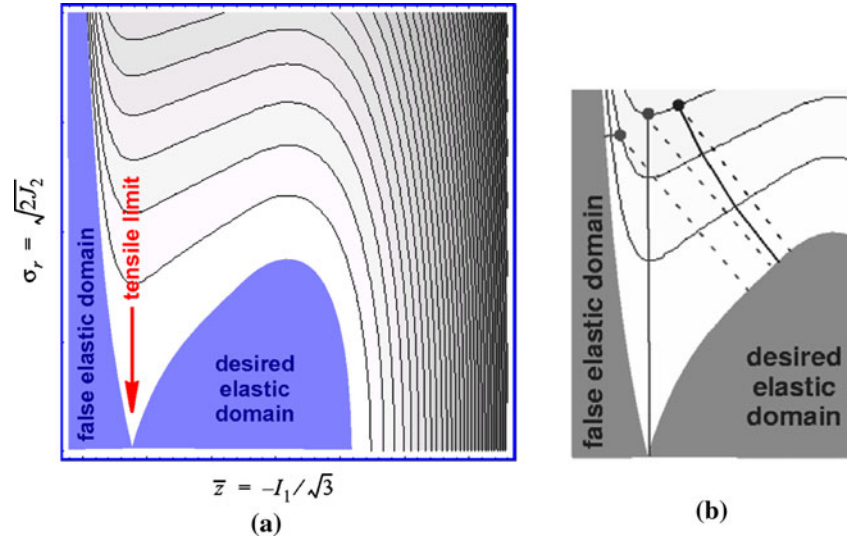
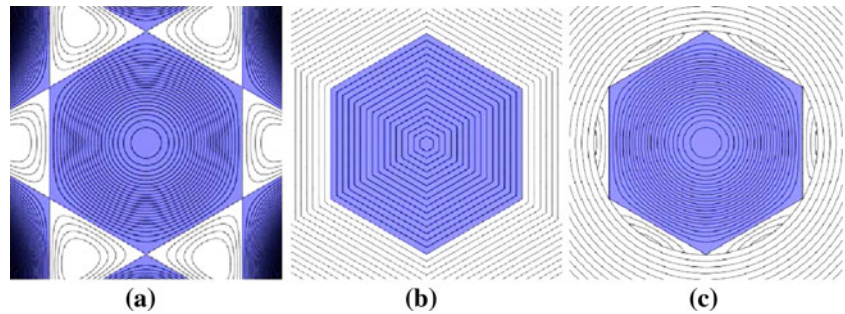


**Fig. 4** Octahedral isosurfaces for **a** the unacceptable Eq. 9 **b** the admissible Eq. 12, and **c** the admissible Eq. 13



projection correction can take the returned state off the yield surface, these steps must be repeated until convergence.

### 3 Pathologies of hardening and flow functions

Let  $F_{ij}$  denote components of the gradient of the yield function with respect to stress  $\sigma_{ij}$ . For an isotropic yield function,  $f(I_1, J_2, J_3)$ ,

$$F_{ij} = \frac{\partial f}{\partial \sigma_{ij}} = \frac{\partial f}{\partial I_1} \frac{\partial I_1}{\partial \sigma_{ij}} + \frac{\partial f}{\partial J_2} \frac{\partial J_2}{\partial \sigma_{ij}} + \frac{\partial f}{\partial J_3} \frac{\partial J_3}{\partial \sigma_{ij}} = \frac{\partial f}{\partial I_1} \delta_{ij} + \frac{\partial f}{\partial J_2} S_{ij} + \frac{\partial f}{\partial J_3} T_{ij}, \tag{14}$$

where  $S_{ij}$  are components of the stress deviator and  $T_{ij}$  are components of the deviatoric part of the square of the stress deviator.

Although yield functions are not unique, their zero isosurface defined by  $f = 0$  is unique (it is the yield surface). Therefore, even though  $F_{ij}$  is not unique, the outward unit normal to the yield surface,

$$N_{ij} = \frac{F_{ij}}{\sqrt{F_{rs} F_{rs}}}, \tag{15}$$

is unique when evaluated on the yield surface.

The stress rate  $\dot{\sigma}_{ij}$  during plastic loading (i.e., when the stress is on the yield surface and remains on the yield surface) is typically governed by

$$\dot{\sigma}_{ij} = \left[ E_{ijkl} - \frac{E_{ijrs} G_{rs} F_{pq} E_{pqkl}}{F_{st} E_{stvw} G_{vw} + h} \right] \dot{\epsilon}_{kl}, \tag{16}$$

where  $\dot{\epsilon}_{kl}$  is the strain rate,  $E_{ijkl}$  is the elastic stiffness,  $h$  is a hardening scalar,  $F_{ij}$  is the gradient of the yield function, and  $G_{ij}$  is defined as

$$G_{ij} = \frac{\partial g}{\partial \sigma_{ij}} \tag{17}$$

in which “ $g$ ” is a flow function. For uncoupled associative plasticity, the flow function is identical to the yield function “ $f$ ”. However, models for cracked and porous media often use non-associative plasticity ( $g \neq f$ ), ostensibly to better match data. Usually, the flow function is taken to have the same form as the yield function, but with different values for the parameters. If, as was done in Eq. 15, we define

$$M_{ij} = \frac{G_{ij}}{\sqrt{G_{rs} G_{rs}}}, \tag{18}$$

then Eq. 16 may be written

$$\dot{\sigma}_{ij} = \left[ E_{ijkl} - \frac{E_{ijrs} M_{rs} N_{pq} E_{pqkl}}{N_{st} E_{stvw} M_{vw} + H} \right] \dot{\epsilon}_{kl}, \tag{19}$$

where the “ensemble hardening modulus”  $H$  is defined (Brannon 2007)

$$H = \frac{h}{\sqrt{F_{rs} F_{rs}} \sqrt{G_{rs} G_{rs}}}. \tag{20}$$

Equation 19 is cast in terms of unique quantities  $M_{rs}$ ,  $N_{pq}$ , and  $H$ . Hence, Eq. 19 is far superior to Eq. 16 which depends on ambiguous tensors  $G_{rs}$  and  $F_{pq}$  and an ambiguous hardening scalar  $h$ . The fact that  $h$  is ambiguous can be demonstrated by recognizing that its formula (not shown) depends on the yield function in a way that causes its value to change if the yield function changes to some other equivalent yield function (i.e., one with the same zero isosurface, but different nonzero isosurfaces). This ambiguity of  $h$  applies for both associative and non-associative plasticity. When performing numerical verification tests, one implementation of a theory agrees with another researcher’s implementation of the same theory only if the ensemble hardening modulus  $H$  in Eq. 20 is the same for both implementations. Unfortunately, this comparison is almost never possible because implementations of plasticity models rarely output values for  $H$ . The hardening scalar  $h$  is devoid of physical meaning because it is affected by ambiguity of yield functions. The ensemble hardening modulus  $H$ , on the other hand, has an appealing physical interpretation: it is the normal displacement of the

yield surface in stress space per unit change in the magnitude of plastic strain. As will be discussed in Sect. 4, this fact can be exploited to find accurate estimates for the location of an evolving yield surface at the end of a plastic step (Brannon 2007).

There are many arguments against non-associativity (Brannon 2007). However, since the physical justifications for the governing equations are not the focus of this paper, we will discuss only the questionable assumption that a flow potential function even exists, because this assumption leads to ambiguity in solving the equations. Like yield functions, flow functions are non-unique. If the algebraic form for a flow function is the same as that of the yield function (but with different parameters), then the only meaningful isosurface of a flow function is the zero isosurface. Ambiguity of the yield function was not disruptive because the governing equations are evaluated only at the yield surface where the corresponding unit normal is unique. However, since a stress located on the zero isosurface of the yield function is not generally at a zero isosurface of the flow function, evaluation of the flow direction  $M_{ij}$  as a gradient of a flow function  $g$  is ambiguous. Whereas  $N_{ij}$  does not change when  $f$  is changed, the flow direction  $M_{ij}$  does change when  $g$  is changed. In fact, an  $M_{ij}$  tensor evaluated using a flow function might change pathologically if the flow function contours are as erratic as those of a typical geomaterial yield function. If one believes that  $M_{ij} \neq N_{ij}$  is truly necessary, then we recommend that  $M_{ij}$  not be evaluated using a flow function. If, for example, a normality rule is found to over-predict dilatation, then an alternative flow model might simply define

$$M_{ij} = \alpha(N_{ij}^{dev} + \beta N_{ij}^{iso}), \tag{21}$$

where  $0 < \beta < 1$  is a control parameter and  $\alpha$  is set to the value necessary to generate a unit tensor. Not only would this approach be more computationally efficient, it would also not be subject to ambiguities of flow functions.

### 4 Nested return algorithm

Note that Eq. 19 may be written

$$\dot{\sigma} = \dot{\sigma}^E - \dot{\Gamma}P \tag{22}$$

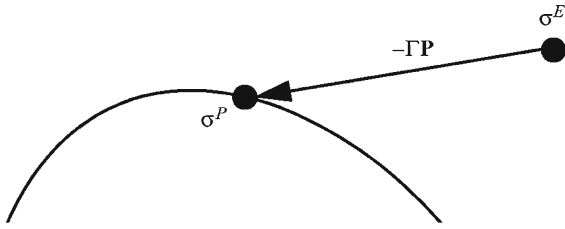


**Fig. 5** Projection of an elastic trial stress to the yield surface along a specified trajectory

where

$$\dot{\sigma}_{ij}^E = E_{ijkl} \dot{\epsilon}_{kl} \tag{23}$$

$$P_{ij} = E_{ijrs} M_{rs} \tag{24}$$

$$\dot{\Gamma} = \frac{N_{pq} E_{pqkl}}{N_{st} E_{stvw} M_{vw} + H} \dot{\epsilon}_{kl}. \tag{25}$$

To first order accuracy, this implies that the stress at the end of a time step must equal the trial elastic stress predictor  $\sigma^E$  minus a corrector  $\Gamma P$ , where the multiple,  $\Gamma = \dot{\Gamma} \Delta t$ , must be selected such that the returned state is on the yield surface. For a non-hardening yield surface, this process is illustrated in Fig. 5. For a hardening yield surface, the multiplier  $\Gamma$  is smaller than that depicted in Fig. 5 to account for expansion of the yield surface under hardening. For a softening yield surface, the multiplier is larger to account for contraction of the yield surface (i.e., loss of strength). This section first addresses how to project to a stationary surface. Then appropriate corrections accounting for motion of the target surface are presented.

For return to a stationary target surface, a nested iterative algorithm is proposed. The algorithm is nested because each of its iterations makes use of a secondary “helper” return algorithm. The helper return algorithm might be, for example, a closest point algorithm or it might be any other existing return algorithm that is recognized to be “flawed” (intentionally or inadvertently) because it fails to return the stress along the required projection direction  $P$ . Presumably, the helper return algorithm is fast and robust. The helper algorithm produces a returned stress  $\sigma^F$  that is not generally the correct solution. To be a correct solution,  $\sigma^E - \sigma^F$  must be a multiple of  $P$ .

If  $\sigma^P$  denotes the desired properly projected stress on the yield surface, then we seek a scalar multiplier  $\Gamma$  (illustrated in Fig. 5) such that

$$\sigma^P = \sigma^E - \Gamma P. \tag{26}$$

The correct value for the multiplier  $\Gamma$  is the zero of the following objective function for a stationary yield surface:

$$g(\Gamma) \equiv f(\sigma^P) = f(\sigma^E - \Gamma P) = 0. \tag{27}$$

A basic (inefficient and non-robust) Newton solver would find  $\Gamma$  by applying the iterator

$$\Gamma_0 = 0; \quad \Gamma_{n+1} = \Gamma_n - \frac{g(\Gamma_n)}{g'(\Gamma_n)} \tag{28}$$

where, by the chain rule,

$$g'(\Gamma) \equiv \frac{dg}{d\Gamma} = \frac{df}{d\sigma^P} : \frac{\partial \sigma^P}{\partial \Gamma} = -G : P. \tag{29}$$

Here,  $G$  is the yield function gradient evaluated at the current estimate for  $\sigma^P$ . In other words,

$$G = \left. \frac{df(\sigma)}{d\sigma} \right|_{\sigma = \sigma^E - \Gamma P}. \tag{30}$$

An efficiency disadvantage of this basic algorithm is that  $\sigma^E$  and  $P$  might not share the same eigenvectors, making it impossible to reduce the dimension of the space in which this sort of return algorithm operates. If a yield function is isotropic, and if  $\sigma$  and  $P$  happen to share the same eigenvectors (which is not generally the case), then it would be possible to return to the yield surface using an algorithm that is cast entirely within 3D principal stress space rather than in the full 6D symmetric tensor space required in the above general algorithm. Of course, even if a 3D iterator were possible, it would still generally require a return trajectory of a particular unique orientation. A basic Newton solver like the one above can also suffer from non-convergence or false-convergence if the yield function has erratic isosurfaces away from the yield surface.

Our goal is to use any existing return iterator (which, in general, will not converge to the correct result but is presumably efficient and robust) as a helper that may be used in the design of a correct nested iterator. Let  $\sigma^F$  denote the converged output of the fast “helper” return iterator. Then  $\sigma^F - \sigma^E$  is not, in general, a multiple of  $P$ . Therefore, even though  $\sigma^F$  is on the yield surface, it is not the solution to Eq. 27 that we seek (i.e.,  $\sigma^F \neq \sigma^P$ ). Below, we assert that an approximation for the correct solution  $\sigma^P$  can be obtained by obliquely projecting  $\sigma^F - \sigma^E$  onto  $P$ .

As illustrated in Fig. 6, it is always possible to write

$$\sigma^P - \sigma^E = (\sigma^P - \sigma^F) + (\sigma^F - \sigma^E). \tag{31}$$

Therefore, letting  $G^F$  denote the yield gradient at the “fast solution” helper state  $\sigma^F$ ,

$$\begin{aligned} (\sigma^P - \sigma^E) : G^F &= (\sigma^P - \sigma^F) : G^F \\ &+ (\sigma^F - \sigma^E) : G^F. \end{aligned} \tag{32}$$

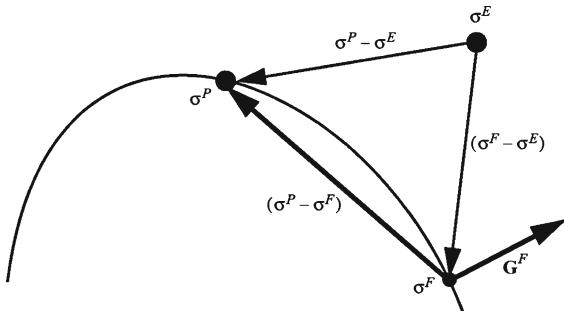


**Fig. 6** Even in this grossly exaggerated sketch, the segment connecting  $\sigma^P$  and  $\sigma^F$  is approximately tangent to the yield surface and therefore approximately perpendicular to the yield surface gradient  $\mathbf{G}^F$

Note from Fig. 6 that  $\sigma^P - \sigma^F$  is approximately tangent to the yield surface and therefore

$$(\sigma^P - \sigma^F) : \mathbf{G}^F \approx 0. \tag{33}$$

This approximation is exact on yield surface flats and becomes increasingly accurate the nearer  $\sigma^F$  is to  $\sigma^P$ .

Noting from Eq. 26 that  $\sigma^P - \sigma^E = -\Gamma \mathbf{P}$ , Eq. 33 may be used to approximate the exact relationship in Eq. 32 by

$$-\Gamma \mathbf{P} : \mathbf{G}^F \approx (\sigma^F - \sigma^E) : \mathbf{G}^F \tag{34}$$

and therefore

$$\Gamma \approx \frac{-(\sigma^F - \sigma^E) : \mathbf{G}^F}{\mathbf{P} : \mathbf{G}^F} \tag{35}$$

and an approximate solution for  $\sigma^P$  therefore follows by substituting this result into Eq. 26. This result motivates the following iterative algorithm for  $\sigma^P$ :

1. Set  $n=0$  and set  $\Gamma_n = 0$  so that  $\sigma^{P_n} = \sigma^{P_0} = \sigma^E$ .
2. Let  $\sigma^{F_{n+1}}$  be the result of any (presumably efficient) return of  $\sigma^{P_n}$  to the yield surface.
3. Compute the yield gradient  $\mathbf{G}^{F_{n+1}}$  evaluated at  $\sigma^{F_{n+1}}$  (and, if desired, also update  $\mathbf{P}$  itself, which typically depends on the normal).
4. Compute  $\Gamma_{n+1}$  using Eq. 35.
5. Then the improved estimate for  $\sigma^P$  is  $\sigma^{P_{n+1}} \approx \sigma^E - \Gamma_{n+1} \mathbf{P}$ .
6. If  $\Gamma_{n+1} - \Gamma_n >$  some tolerance, then set  $n = n + 1$ , and go to step 2. Otherwise exit with the converged solution given by  $\Gamma = \Gamma_{n+1}$ .

As long as solutions exist for both  $\sigma^P$  and  $\sigma^F$ , convexity of the yield surface ensures that the denominator  $\mathbf{P} : \mathbf{G}^F$  in the formula for  $\Gamma$  will be positive. The algorithm would diverge if, at any point,  $\Gamma$  evaluates to a

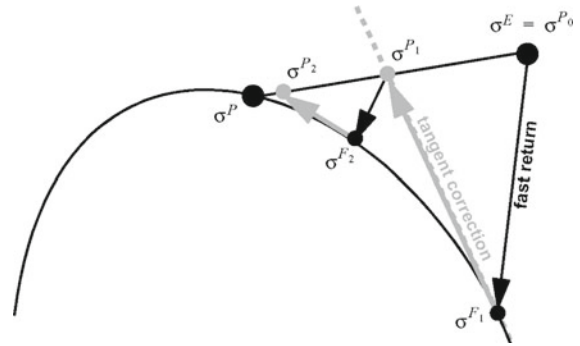


**Fig. 7** Two iteration cycles in which an incorrect (but presumably efficient) “helper” solution  $\sigma^F$  is projected onto the required unique level set to obtain an estimate of the actual solution  $\sigma^P$ . This figure illustrates that nested convergence is extremely rapid even when the fast helper solution is grossly inaccurate and even when the yield surface is highly curved

negative number, but this will not occur so long as the helper algorithm does not “cut across” elastic states to find the second solution that always exists on the other side of the convex yield surface.

Interpreted geometrically, Eq. 35 implies that the segment connecting  $\sigma^P$  and  $\sigma^F$  is approximately a type-1 oblique projection of the segment connecting  $\sigma^F$  and  $\sigma^E$  onto the level set defined by  $\mathbf{P}$ . Hence, as illustrated in Fig. 7, each iteration treats the current estimate for  $\sigma^P$  as if it were  $\sigma^E$ . The stress that is predicted by the (presumably fast and robust) “helper” return algorithm is simply projected onto the required level set following a path that is tangent to the yield surface.

This nested iterator converges in one step whenever Eq. 33 holds exactly. This will occur whenever the fast helper solution  $\sigma^F$  happens to hit on the exact solution  $\sigma^P$  or whenever  $\sigma^F$  and  $\sigma^P$  happen to reside on a flat portion of the yield surface. Otherwise, as should be clear from Fig. 7, the number of nested iterations increases with increasing yield surface curvature. The closer the fast iterator can come to the exact solution, the faster the nested iterator will be. This concludes the discussion of return to a stationary yield surface.

For hardening or softening, the yield surface evolves in response to changes in the internal state variables (ISVs). The rate form of the governing equation continues to be of the form in Eq. 22 and therefore, the updated stress is still of the form in Eq. 26. The multiple  $\Gamma$  must still be selected such that the updated stress is on the updated yield surface. However, the updated location of the yield surface is unknown because it

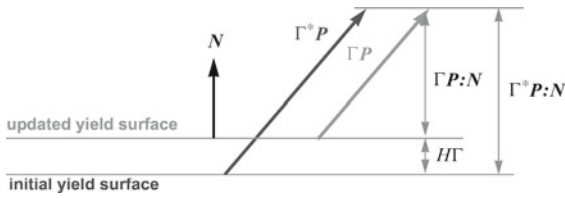


**Fig. 8** Using the plastic strain increment ( $\Gamma^*$ ) from non-hardening to determine the actual increment ( $\Gamma$ ) with hardening (Brannon 2007)

depends on the amount of change in the ISVs during the time step. The magnitude of the plastic strain increment, which is needed to update the ISVs, is actually the unknown multiplier  $\Gamma$ .

This problem of needing to project to a surface whose location is unknown can be solved by considering the geometric meaning of the consistency equation, which is the equation requiring stress to remain on the evolving yield surface during plastic loading increments. When using unit normal and unit flow direction tensors,  $N$  and  $M$ , the consistency equation is

$$\dot{\sigma} : N = H \dot{\Gamma} \tag{36}$$

where  $H$  is the ensemble hardening modulus in Eq. 20 and  $\dot{\Gamma}$  is the magnitude of the plastic strain rate defined in Eq. 25. Because the normal in this equation is a unit tensor and because the stress is moving with the yield surface, the left-hand-side of this equation is the normal velocity of the yield surface in stress space. Therefore, multiplying by the timestep  $\Delta t$  gives a first-order approximation to the normal displacement of the yield surface during the time step, as labeled in Fig. 8.

Equating distances labeled in Fig. 8 and solving for  $\Gamma$  gives

$$\Gamma = \Gamma^* \frac{(P : N)}{P : N + H}. \tag{37}$$

Here,  $\Gamma^*$  is the  $\Gamma$  multiplier that returns the elastic trial stress state to the yield surface at the beginning of the step (which is at a particular instant in time and therefore stationary). Once  $\Gamma$  has been found, the plastic strain and internal variables can be immediately updated. For example,  $\Delta \epsilon^p = \Gamma M$ .

### 5 Proposed case studies for algorithm verification

For simple preliminary verification of the proposed algorithm, the two-stage return algorithm was implemented as a user-defined routine in a commercial

finite element code, LS-DYNA. Three case studies are considered. Solutions are obtained from single-element simulations using LS-DYNA, and compared with closed-form analytical solutions. Each case study is described below, starting with a complicated problem having time-varying principal stress directions without changes in principal stresses. Then the next example involves time-varying principal stresses without changes in principal directions. Both of these examples allow verification of the algorithm in situations where the stress must move along a curved trajectory to remain on the curved yield surface. The final example, which is probably the easiest, is a non-associative linear Drucker–Prager problem that allows verification that the correct return direction has been enforced.

#### Example 1 Transient stress eigenvectors with stationary eigenvalues

For the return to a stationary surface, a distinguishing feature of the two stage algorithm is that it allows for the possibility that the elastic trial stress and the updated stress might have different eigenvectors. Therefore, this section presents the analytical derivation of a manufactured solution (Roache 1998) that is used in a simulation to verify the proposed nested return algorithm. By design, this problem involves significant changes in the principal stress directions without changes in the eigenvalues. This problem serves as a verification problem for implementation of the nested return algorithm that is more challenging than simple monotonic loading problems. In this verification problem, the material is subjected to a strain rate that, by design, will cause the eigenvectors of the stress tensor to change during plastic loading while not changing the eigenvalues.

Consider a non-hardening linear Drucker–Prager material whose yield criterion is given by

$$r = r_y - (\tan \phi)z, \tag{38}$$

where  $r_y$  and  $\phi$  are material constants and

$$r \equiv \sqrt{2J_2} = \sqrt{S_{ij}S_{ij}} \quad \text{and} \quad z \equiv \frac{I_1}{\sqrt{3}} = \frac{\sigma_{kk}}{\sqrt{3}}. \tag{39}$$

We will assume normality. Then, taking the yield function to be  $f = r \cos \phi + z \sin \phi - r_y \cos \phi$ , the flow direction equals the unit normal to the yield surface, given by

$$M = N = (\cos \phi)\hat{S} + (\sin \phi)\hat{I}, \tag{40}$$

where  $\hat{S}$  is a unit tensor in the direction of  $S$ , and  $\hat{I}$  is similarly a unit tensor in the direction of the identity tensor  $I$ . Specifically,

$$\hat{S} = \frac{S}{\|S\|} \quad \text{and} \quad \hat{I} = \frac{I}{\|I\|} = \frac{I}{\sqrt{3}}. \tag{41}$$

Assuming linear elasticity (shear modulus  $G$  and bulk modulus  $K$ ) and no elastic-plastic coupling, the projection direction tensor is then

$$P = E : M = (2G \cos \phi)\hat{S} + (3K \sin \phi)\hat{I} \tag{42}$$

For simplicity of the analysis, we use the following values for the material properties:

Shear modulus:  $G = 500$  MPa

Poisson's ratio:  $\nu = \frac{1}{3}$

Bulk modulus:  $K = \frac{4,000}{3}$  MPa

Yield parameters:

$$r_y = 5 \text{ MPa}, \quad \cos \phi = \frac{4}{5}, \quad \sin \phi = \frac{3}{5}$$

Using these parameters, it follows that

$$M = N = \frac{4\hat{S} + 3\hat{I}}{5} \tag{43}$$

$$P = E : M = 800(\hat{S} + 3\hat{I}) \text{ MPa} \tag{44}$$

For this problem, the first (elastic) leg loads to the yield surface using isochoric (volume preserving) axisymmetric compression in which both the stress and strain tensors are multiples of

$$\begin{bmatrix} -2 & 0 & 0 \\ 0 & 1 & 0 \\ 0 & 0 & 1 \end{bmatrix}. \tag{45}$$

More generally, this is the principal component matrix for any tensor that is a positive multiple of

$$I - 3nn \tag{46}$$

where  $n$  is the axisymmetry axis and the second order tensor  $nn$  is a dyad (i.e., its  $ij$  component is  $n_i n_j$ ). Equation 45 is a special case of Eq. 46 obtained by choosing  $n$  to point in the 1-direction. The magnitude of the tensor in Eq. 46 is  $\sqrt{6}$ . Therefore, letting  $r = \sqrt{2J_2}$  denote the magnitude of the stress deviator, the stress tensor can be written in the form

$$\sigma = \frac{r}{\sqrt{6}}(I - 3nn) \tag{47}$$

and the associated elastic strain tensor is

$$e^e = \frac{\sigma}{2G}. \tag{48}$$

The rate of the stress tensor is

$$\dot{\sigma} = \frac{\dot{r}}{\sqrt{6}}(I - 3nn) - \sqrt{\frac{3}{2}}r(\dot{n}n + n\dot{n}) \tag{49}$$

In this section, we design a total strain history ensuring that the stress remains always of the form in Eq. 47. The strain history consists of two legs: an elastic loading to the yield surface, followed by plastic loading. During the elastic leg, the symmetry axis  $n$  is held fixed. The elastic leg ends at a pre-selected time  $t_y$ . During the plastic leg,  $r$  is held fixed at  $r_y$ , but the principal stress directions are made to vary by rotating the symmetry axis  $n$ . In particular, we design a total strain history such that the symmetry axis is of the form

$$n = \begin{cases} e_1 & \text{during elastic leg} \\ \cos(\omega T)e_1 + \sin(\omega T)e_2 & \text{during plastic leg} \end{cases} \tag{50}$$

where  $e_k$  denotes the  $k^{\text{th}}$  laboratory basis vector,  $\omega$  is the angular velocity and  $T = t - t_y$ . We design the total strain history such that

$$\omega = \begin{cases} 0 & \text{during elastic leg} \\ \text{constant} & \text{during plastic leg} \end{cases} \tag{51}$$

and

$$r = \begin{cases} r_y \left(\frac{t}{t_y}\right) & \text{during elastic leg} \\ r_y & \text{during plastic leg} \end{cases} \tag{52}$$

Because the stress is, by design, always deviatoric, the associated elastic strain is found simply by dividing the stresses by  $2G$ . Thus,

$$e^e = \frac{r}{2G\sqrt{6}}(I - 3nn). \tag{53}$$

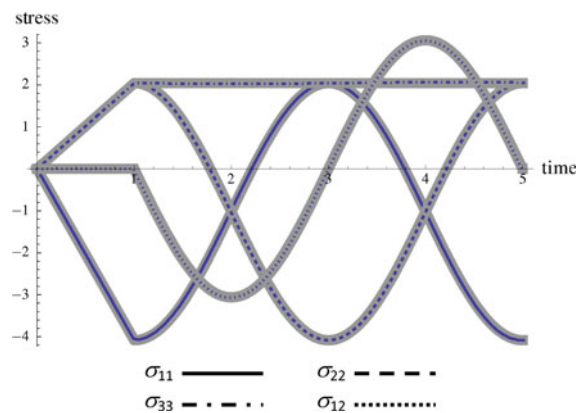


**Fig. 9** Solution corresponding to the driving strains as described in Example 1. The analytical results *thick lines* are shown along with a numerical simulation from LS-DYNA using a user-defined model with nested return algorithm (*thin black lines*)

The elastic strain history associated with a prescribed stress history is determined uniquely (as we have done here) by applying Hooke’s law. However, for non-hardening plasticity, the plastic strain history is not uniquely determined from the stress history. For our reverse engineered design of a total strain history, we will seek a plastic strain history for which the magnitude of the plastic strain rate tensor is a specified constant  $a$ . Then the plastic strain rate must be given by

$$\mathbf{M} = \mathbf{N} = (\cos \phi)\hat{\mathbf{S}} + (\sin \phi)\hat{\mathbf{I}} \tag{54}$$

$$\dot{\boldsymbol{\epsilon}}^P = a\mathbf{M} \tag{55}$$

or, using Eqs. 40 and 47,

$$\dot{\boldsymbol{\epsilon}}^P = a \left( \frac{\cos \phi}{\sqrt{6}}(\mathbf{I} - 3\mathbf{m}\mathbf{m}) + (\sin \phi)\frac{\mathbf{I}}{\sqrt{3}} \right) \tag{56}$$

During the plastic leg, the only time varying part of the above equation is the dyad  $\mathbf{m}\mathbf{m}$ , which, in matrix form is

$$[\mathbf{m}\mathbf{m}] = \frac{1}{2} \begin{bmatrix} 1 + \cos(2\omega T) & \sin(2\omega T) & 0 \\ \sin(2\omega T) & 1 - \cos(2\omega T) & 0 \\ 0 & 0 & 0 \end{bmatrix}. \tag{57}$$

This tensor, along with the constant tensors in Eq. 56 is easily integrated through time to obtain a time history for the plastic strain tensor  $\boldsymbol{\epsilon}^P(t)$ , which may then be added to the time varying elastic strain tensor in Eq. 53 to ultimately obtain the time varying total strain tensor that will produce the stress history and equivalent plastic strain rate that we seek. The stresses corresponding to the driving strains in this problem are shown in Fig. 9. The exact solution is represented by the thick lines while the thin black lines represent the solution obtained from a single-element simulation using the proposed nested return algorithm.

The functions in Table 1 give the components of tensors with respect to a fixed basis  $\{e_1, e_2, e_3\}$ , which are the components that would be computed in a plasticity code. These functions are plotted in the left-hand column of Fig. 10. The right hand column shows the tensor components with respect to a basis  $\{e_1^*, e_2^*, e_3^*\}$  that is defined such that  $e_1^*$  is aligned with the compression symmetry axis  $\mathbf{n}$ . With respect to this rotated “star” basis, a tensor component  $Y_{ij}^*$  is  $e_i^* \cdot \mathbf{Y} \cdot e_j^*$ . Less trivially,  $\dot{Y}_{ij}^* = e_i^* \cdot \dot{\mathbf{Y}} \cdot e_j^*$ , which is not the same as  $dY_{ij}^*/dt$ . Given that the stress invariants remain constant, the stress will appear to be stationary in principal stress space upon reaching yield. However, the stress varies because its principal directions change.

The span of the following tensors defines a 3D manifold in 6D symmetric tensor space:

$$\begin{bmatrix} -1 & 0 & 0 \\ 0 & 1 & 0 \\ 0 & 0 & 0 \end{bmatrix} \quad \begin{bmatrix} 0 & -1 & 0 \\ -1 & 0 & 0 \\ 0 & 0 & 0 \end{bmatrix} \quad \begin{bmatrix} -1 & 0 & 0 \\ 0 & -1 & 0 \\ 0 & 0 & 2 \end{bmatrix} \tag{58}$$

Throughout the duration of this problem (both elastic and plastic legs), the stress tensor may be expressed as a linear combination of the above three tensors. Letting  $\{\sigma_A, \sigma_B, \sigma_C\}$  denote the projection of the stress tensor onto these three tensors gives a time varying triplet of numbers that may be plotted parametrically as shown in Fig. 11 to demonstrate that the stress state is moving in a circle in 6D tensor space even though it is stationary in principal stress space.

*Example 2* Transient stress eigenvalues with stationary eigenvectors

This example solves non-hardening von Mises plasticity equations for the case of a constant strain rate that is not aligned with the yield normal (see Fig. 12). This example demonstrates that the nested return algorithm can still project the stress to the correct position despite the presence of the curvature. The strain path is chosen such that the stress deviator is rotated. The material parameters and a simple piecewise linear strain table in which the strain eigenvectors are fixed are presented in Tables 2 and 3, respectively. Here, the structure is first loaded under triaxial extension (TXE) until the stress reaches yield. The strain is then steered away from the TXE state into other Lode angles.

The exact solution for the stress (MPa) is (Krieg and Krieg 1977; Kossa and Szabó 2009)

$$\sigma_{11} = \begin{cases} -474.0t & \text{if } 0 < t \leq 0.201 \\ -95.26 & \text{if } 0.201 < t \leq 1 \\ \frac{189.4+0.1704\sqrt{a}-0.003242a}{1+0.00001712a} & \text{if } 1 < t \leq 2 \\ 189.4 & \text{as } t \rightarrow \infty \end{cases} \tag{59}$$

$$\sigma_{22} = \begin{cases} -474.0t & \text{if } 0 < t \leq 0.201 \\ -95.26 & \text{if } 0.201 < t \leq 1 \\ \frac{76.87+1.443\sqrt{a}-0.001316a}{1+0.00001712a} & \text{if } 1 < t \leq 2 \\ 76.87 & \text{as } t \rightarrow \infty \end{cases} \tag{60}$$

**Table 1** Example 1: solution table

	Elastic leg $0 < t < 1$	Plastic leg $1 < t < 5$
$\varepsilon_{11}$	$\frac{-2t}{200\sqrt{6}}$	$\frac{6\sqrt{2} \cos\left(\frac{\pi t}{2}\right) - \pi \left[3 + 4\sqrt{2} - 3t + \sqrt{2}t + 15\sqrt{2} \sin\left(\frac{\pi t}{2}\right)\right]}{4000\sqrt{3}\pi}$
$\varepsilon_{22}$	$\frac{t}{200\sqrt{6}}$	$\frac{6\sqrt{2} \cos\left(\frac{\pi t}{2}\right) + \pi \left[3 + 4\sqrt{2} - 3t + \sqrt{2}t - 15\sqrt{2} \sin\left(\frac{\pi t}{2}\right)\right]}{4000\sqrt{3}\pi}$
$\varepsilon_{33}$	$\frac{t}{200\sqrt{6}}$	$\frac{-3 + 8\sqrt{2} + (3 + 2\sqrt{2})t}{4000\sqrt{3}}$
$\varepsilon_{12}$	0	$\frac{\sqrt{3}(-2 + 5\pi \cos\left(\frac{\pi t}{2}\right) + 2 \sin\left(\frac{\pi t}{2}\right))}{2000\sqrt{2}\pi}$
$\dot{\varepsilon}_{11}^e$	$\frac{-2}{200\sqrt{6}}$	$-\frac{1}{800}\sqrt{\frac{3}{2}}\pi \cos\left(\frac{\pi t}{2}\right)$
$\dot{\varepsilon}_{22}^e$	$\frac{1}{200\sqrt{6}}$	$\frac{1}{800}\sqrt{\frac{3}{2}}\pi \cos\left(\frac{\pi t}{2}\right)$
$\dot{\varepsilon}_{33}^e$	$\frac{1}{200\sqrt{6}}$	0
$\dot{\varepsilon}_{12}^e$	0	$-\frac{1}{800}\sqrt{\frac{3}{2}}\pi \sin\left(\frac{\pi t}{2}\right)$
$\dot{\varepsilon}_{11}^p$	0	$-\frac{-3 + \sqrt{2} + 3\sqrt{2} \sin\left(\frac{\pi t}{2}\right)}{4000\sqrt{3}}$
$\dot{\varepsilon}_{22}^p$	0	$-\frac{\sqrt{\frac{2}{3}} + \sqrt{3} + \sqrt{6} \sin\left(\frac{\pi t}{2}\right)}{4000}$
$\dot{\varepsilon}_{33}^p$	0	$\frac{(3 + 2\sqrt{2})}{4000\sqrt{3}}$
$\dot{\varepsilon}_{12}^p$	0	$\frac{\sqrt{\frac{3}{2}} \left[\cos\left(\frac{\pi t}{2}\right)\right]}{2000}$
$\sigma_{11}$ MPa	$-5t\sqrt{\frac{2}{3}}$	$-5 \left[3 \sin\left(\frac{\pi t}{2}\right) + 1\right]$
$\sigma_{22}$ MPa	$\frac{5t}{\sqrt{6}}$	$\frac{5 \left[3 \sin\left(\frac{\pi t}{2}\right) - 1\right]}{2\sqrt{6}}$
$\sigma_{33}$ MPa	$\frac{5t}{\sqrt{6}}$	$\frac{5}{\sqrt{6}}$
$\sigma_{12}$ MPa	0	$\frac{5}{2}\sqrt{\frac{3}{2}} \cos\left(\frac{\pi t}{2}\right)$
$\dot{\lambda} = \ \dot{\varepsilon}^p\ $	0	$\frac{1}{800}$
$N_{11}$	$\frac{1}{15} (3\sqrt{3} - 4\sqrt{6})$	$-\frac{-3 + \sqrt{2} + 3\sqrt{2} \sin\left(\frac{\pi t}{2}\right)}{5\sqrt{3}}$
$N_{22}$	$\frac{3 + 2\sqrt{2}}{5\sqrt{3}}$	$\frac{1}{5} \left[-\sqrt{\frac{2}{3}} + \sqrt{3} + \sqrt{6} \sin\left(\frac{\pi t}{2}\right)\right]$
$N_{33}$	$\frac{3 + 2\sqrt{2}}{5\sqrt{3}}$	$\frac{3 + 2\sqrt{2}}{5\sqrt{3}}$
$N_{12}$	0	$\frac{1}{5}\sqrt{6} \cos\left(\frac{\pi t}{2}\right)$
$P_{11}$ MPa	$\frac{800(-3 + \sqrt{2})}{\sqrt{3}}$	$\frac{200 \left[-12 + \sqrt{2} - 3\sqrt{2} \sin\left(\frac{\pi t}{2}\right)\right]}{\sqrt{3}}$
$P_{22}$ MPa	$\frac{400(6 + \sqrt{2})}{\sqrt{3}}$	$\frac{200 \left[12 - \sqrt{2} + 3\sqrt{2} \sin\left(\frac{\pi t}{2}\right)\right]}{\sqrt{3}}$

**Table 1** continued

	Elastic Leg $0 < t < 1$	Plastic Leg $1 < t < 5$
$P_{33}$ MPa	$\frac{400(6 + \sqrt{2})}{\sqrt{3}}$	$\frac{400(6 + 2\sqrt{2})}{\sqrt{3}}$
$P_{12}$ MPa	0	$200\sqrt{6} \cos\left(\frac{\pi t}{2}\right)$

$$\sigma_{33} = \begin{cases} 948.0t & \text{if } 0 < t \leq 0.201 \\ 190.5 & \text{if } 0.201 < t \leq 1 \\ \frac{-112.5 + 1.272\sqrt{a} - 0.001926a}{1 + 0.00001712a} & \text{if } 1 < t \leq 2 \\ 112.5 & \text{as } t \rightarrow \infty, \end{cases} \quad (61)$$

where  $a = e^{12.33t}$ . The comparison of the computed stresses are shown in Fig. 13.

*Example 3* Single-element test for a linear Drucker–Prager yield with nonassociativity

Similar to Example 1, a linear Drucker-Prager yield function of the following form is considered,

$$f = \frac{r}{r_0} + \frac{z}{z_0}. \quad (62)$$

The parameters and strain path used in this example are given in Tables 4 and 5. The strain path for this example is devised such that the first two yield events occur exactly halfway through the second and third legs. Moreover, as illustrated in Fig. 14, the strain path is designed so that the trial elastic stress rate will be exactly parallel to the return projection direction in the second leg and it will be exactly parallel to the yield surface normal in the third leg. The exact solution to this problem is given in Table 6. Figure 15 shows the comparison of stresses obtained from the exact solution and the single-element simulation using a user-defined routine with nested algorithm implemented in LS-DYNA.

### 6 Discussion and conclusions

This paper has called attention to pathological shapes of yield function contours (isosurfaces) and violations of yield-function sign conventions that are often inadvertently present in typical in engineering models for cracked and porous media. This topic is important

because numerical return algorithms rely on the yield-function sign convention to decide if a trial stress state is outside the yield surface, and because numerical return algorithms rely on well-behaved yield contours to return the trial stress to the yield surface. Some simple strategies were discussed for handling pathological yield functions in numerical solvers.

To circumvent difficulties associated with pathological yield function contours, and also to improve numerical efficiency, a multi-stage return algorithm for solving the classical damage component of constitutive models for rocks and rock-like media was proposed. Using an incorrect, but presumably more straightforward fast return iterator, the nested iterator is designed to apply a correction that mitigates problems that can occur under large excursions of the trial stress state from the yield surface. Such issues are particularly relevant in softening problems because the yield surface can collapse in such a way that return algorithms have difficulty locating the damaged surface. The two-stage return algorithm allows using a robust return to the yield or limit surface at the beginning of a time step as a helper in finding the returned state at a softened yield surface at the end of the step. Since the helper return algorithm is robust (i.e., it always finds a point on the yield surface), the only means of non-convergence is potentially oscillating solutions in the correction step, as is also a risk with Newton solvers.

The proposed multi-stage return algorithm is also applicable to hardening. It is particularly attractive because it can be used to improve existing return algorithms that are robust but inaccurate because they employ an incorrect return direction. The second stage of the return algorithm is a correction of a predictor obtained using a presumably efficient and robust return algorithm.

The correction is exact if the yield surface is flat. Otherwise, the corrected stress state is used as the starting point for calling the original (fast, but incorrect)

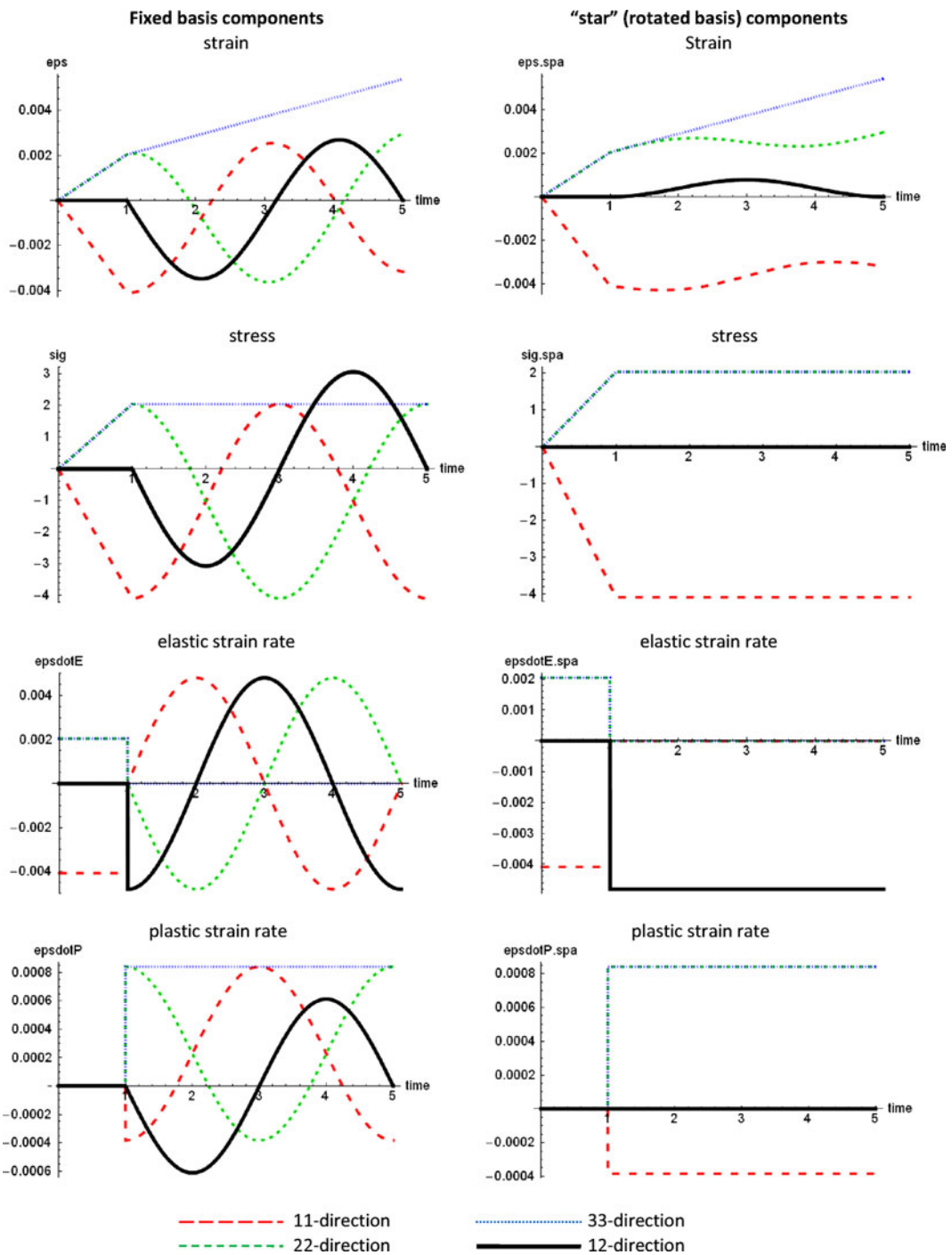


**Fig. 10** Comparison of the fixed basis tensor components *left column* with components as seen by an observer rotating with  $n$  *right column*. The differences illustrate that the rotation of principal stress directions cannot be interpreted as merely a basis

change of a fixed axis problem. The two are fundamentally different. The stress invariants remain constant after reaching yield, but the stress tensor itself is not constant because its principal directions change

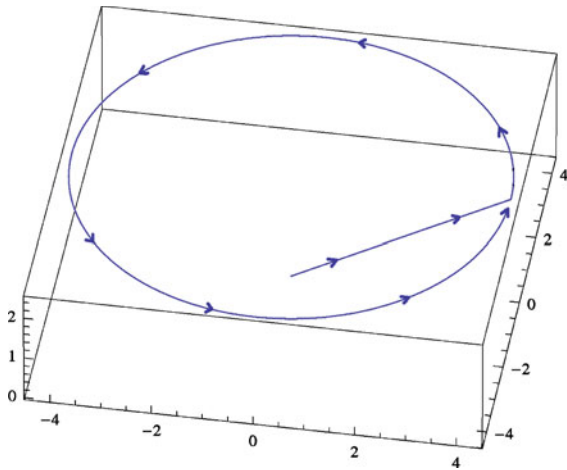


**Fig. 11** Stress trajectory in the 3D submanifold spanned by the tensors in Eq. 58. After yielding, the stress moves along a circular path in this space that, despite appearances, should not be confused with the octahedral plane in principal stress space. There is no motion of the stress in the octahedral plane. Motion of the stress in this plot occurs because the octahedral plane *itself* varies in time

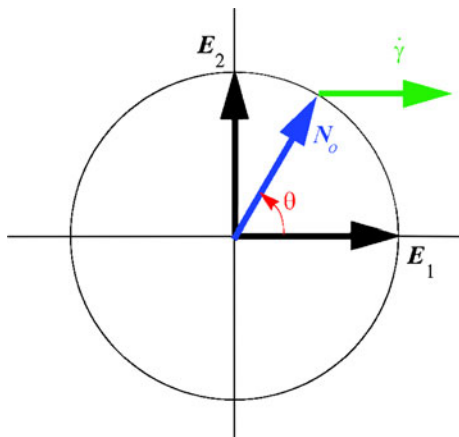


**Fig. 12** Example 2: von Mises Plasticity under a constant strain rate  $\dot{\gamma}$ .  $E_1$  is a unit tensor in the direction of the strain rate deviator.  $E_2$  is a unit tensor orthogonal to  $E_1$ .  $N_0$  is a unit tensor in the direction of the initial stress deviator

**Table 2** Example 2: material parameters

Parameter	Value
Yield in shear, $\tau_y$	165 MPa
Shear modulus, $G$	79 GPa

return algorithm, and applying the projection again. The fast return function might return the stress to an incorrect location either inadvertently (because of a

**Table 3** Example 2: strain table

Time (s)	$\epsilon_{11}$	$\epsilon_{22}$	$\epsilon_{33}$
0	0	0	0
1	-0.003	-0.003	0.006
2	-0.0103923	0	0.0103923

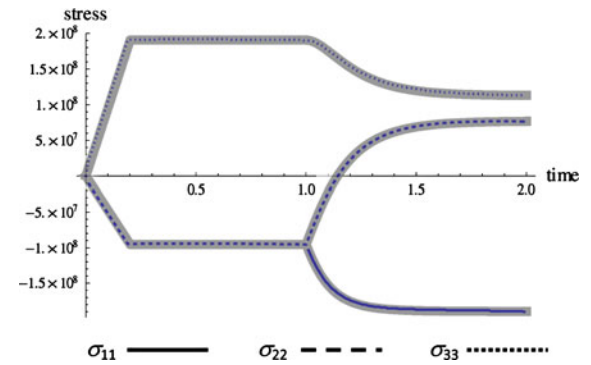


**Fig. 13** The solution to the von Mises plasticity problem defined in Example 2. The *thick colored lines* are the analytical solution. The *thin black lines* that overlay the exact solution a results from a user-defined routine with nested return algorithm implemented in LS-DYNA

**Table 4** Example 3: model parameters

Parameter	Value
Bulk modulus, $K$	10,000
Poisson's ratio, $\nu$	1/3
Young's modulus, $E$	10,000
Shear modulus, $G$	3,750
Lame modulus, $\lambda$	7,500
$r_0$	50
$z_0$	$50\sqrt{3}$
Yield normal, $N$	$\frac{3S + I}{2\sqrt{3}}$
Flow direction, $M$	$\frac{6S + I}{\sqrt{39}}$

**Table 5** Example 3: strain table

Time (s)	$\epsilon_{11}$	$\epsilon_{22}$	$\epsilon_{33}$
0	0	0	0
1	-0.009444	-0.009444	-0.009444
2	-0.04410	0.02122	0.02122
3	0.02788	-0.004776	-0.004776

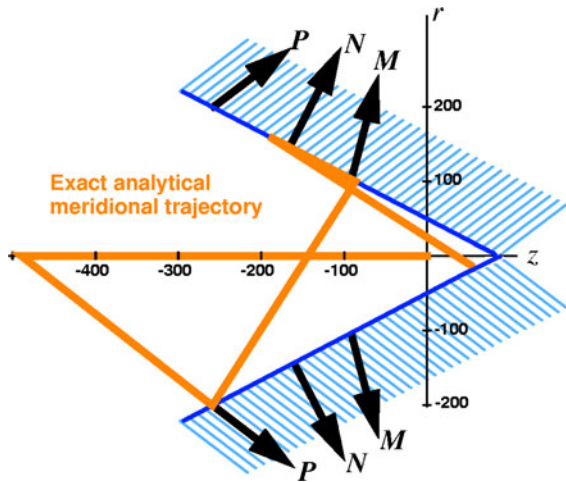


**Fig. 14** Stress trajectory in  $r$ - $z$  space for Example 3. The path begins at the origin with an initial hydrostatic leg. The second leg might appear to only briefly touch the yield surface, but it is actually stagnating under extended plastic deformation. Alignment of the trial stress rate with  $P$  during that leg ensures that there is no motion in stress space

theoretical oversight) or intentionally. In the latter category, for example, the fast return algorithm might be a simple radial return that scales down the magnitude of the stress deviator, and then the superimposed iterator projects this result onto the correct return direction. In this case, the fast iterations are in one dimension (possibly even analytical if the yield function is simple enough), while the projection is generally applied in 6D

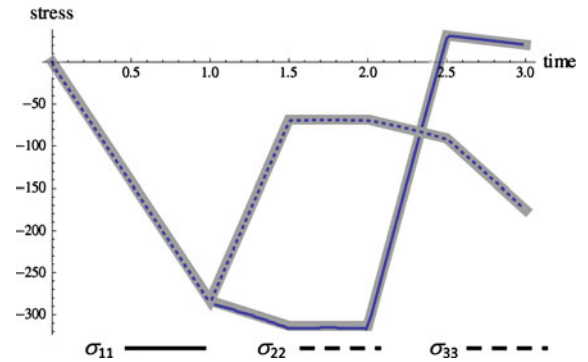


**Fig. 15** Solution corresponding to the driving strains prescribed in Table 5. The analytical results (*thick lines*) are shown along with a numerical simulation from LS-DYNA using a user-defined model with nested return algorithm (*thin black lines*)

stress space. By eliminating numerous higher dimensional iterations, the nested algorithm can potentially boost efficiency.

To date, the nested return algorithm and masking of pathological yield contours have been implemented and confirmed in a standard suite of over 30 benchmark problems, several of which include analytical solutions. This paper has presented additional case studies that compare the numerical solver with analytical solutions. Two of these case studies involved motion of the stress around regions of curvature, either from the rotation of the principal stress directions with no motion in principal stress space or vice versa. The final case study allowed verification of a proper return direction under non-associative plasticity.

**Table 6** Example 3: solution table

Leg	End time	Reason for ending leg	$\epsilon_{11}$	$\epsilon_{22}, \epsilon_{33}$	$\sigma_{11}$	$\sigma_{22}$	$\sigma_{22}$
1E	1	Change in prescribed strain rate	$-\frac{17}{1800}$	$-\frac{17}{1800}$	$-\frac{850}{3}$	$-\frac{850}{3}$	$-\frac{850}{3}$
2E	$\frac{3}{2}$	Yield	$-\frac{9 + 16\sqrt{6}}{1800}$	$-\frac{9 - 8\sqrt{6}}{1800}$	$-\frac{50}{3}(9 + 4\sqrt{6})$	$\frac{50}{3}(2\sqrt{6} - 9)$	$\frac{50}{3}(2\sqrt{6} - 9)$
2P	2	Change in prescribed strain rate	$-\frac{1 + 32\sqrt{6}}{1800}$	$-\frac{1 - 16\sqrt{6}}{1800}$	$-\frac{50}{3}(9 + 4\sqrt{6})$	$\frac{50}{3}(2\sqrt{6} - 9)$	$\frac{50}{3}(2\sqrt{6} - 9)$
3E	$\frac{5}{2}$	Yield	$\frac{5 - 8\sqrt{6}}{1800}$	$\frac{5 + 4\sqrt{6}}{1800}$	$\frac{50}{3}(2\sqrt{6} - 3)$	$-\frac{50}{3}(3 + \sqrt{6})$	$-\frac{50}{3}(3 + \sqrt{6})$
3P	2	Change in prescribed strain rate	$\frac{11 + 16\sqrt{6}}{1800}$	$\frac{11 - 8\sqrt{6}}{1800}$	$160\sqrt{\frac{2}{3}} - 110$	$-\frac{10}{3}(33 + 8\sqrt{6})$	$-\frac{10}{3}(33 + 8\sqrt{6})$

**Acknowledgments** Support of this work by the Engineering Sciences Research Foundation (ESRF) under the direction of J. Guadalupe Argüello, Mike Stone, and Erik Strack at Sandia National Laboratories is gratefully acknowledged. Helpful insights from the reviewers and from our colleague, Mataz Alcoulabi, have significantly improved the paper.

## References

- ASME V&V 10-2006 (2006) Guide for verification and validation in computational solid mechanics. The American Society of Mechanical Engineers, New York, NY
- Bicanic N, Pearce CJ (1998) Computational aspects of a softening plasticity model for plain concrete. *Mech Cohesive-Frict Mat* 1:75–94
- Brannon RM (2007) Elements of phenomenological plasticity: geometrical insight, computational algorithms, and topics in shock physics. *Shock Wave Science and Technology Reference Library*, vol. 2, chap. 6. Springer, Berlin, pp 225–274
- Brannon RM, Wells JM, Strack O (2007) Validating theories for brittle damage. *Metall Mater Trans A* 38(12):2861–2868
- Fossum AF, Brannon RM (2004) The SANDIA GEOMODEL theory and user's guide. Sandia National Laboratories Report SAND2004-3226, Albuquerque (unlimited release edn)
- Foster CD, Regueiro RA, Fossum AF, Borja RI (2005) Implicit numerical integration of a three-invariant, isotropic/kinematic hardening cap plasticity model for geomaterials. *Comput Methods Appl Mech Eng* (194): 5109–5138
- Kossa A, Szabó L (2009) Exact integration of the von Mises elastoplasticity model with combined linear isotropic-kinematic hardening. *Int J Plasticity* 25:1083–1106
- Krieg RD, Krieg DB (1977) Accuracies of numerical solution methods for the elastic-perfectly plastic model. *J Press Vessel Technol* 99:510–515
- Lubliner J (1990) *Plasticity theory*. Macmillan, New York
- Roache PJ (1998) *Verification and validation in computational science and engineering*. Hermosa Publishers, Albuquerque
- Sandler IS, Rubin D (1979) An algorithm and a modular subroutine for the cap model. *Int J Numer AnalMethods Geomech* 3:173